JOURNAL OF GEOPHYSICAL RESEARCH, VOL. 100, NO. C9, PAGES 18,503–18,515, SEPTEMBER 15, 1995

Circulation and transport of water along the western Weddell Sea margin

Robin D. Muench[1]
Earth & Space Research, Seattle, Washington

Arnold L. Gordon
Lamont-Doherty Earth Observatory, Palisades, New York

Abstract. Ocean current, temperature, and salinity data obtained from the western Weddell Sea during the austral winter 1992 U.S.-Russian drifting ice station experiment Ice Station Weddell 1 (ISW-1) are used to describe water circulation and transport. Surface-to-bottom baroclinic currents were computed by applying the geostrophic approximation to derived density data. These were corrected using current measurements obtained from drifting current meter arrays, and the resulting total currents were vertically integrated to obtain volume transports. Transport was found to be northward in the region, which encompassed the western boundary current of the cyclonic Weddell Sea gyre. This northward transport increased from south to north by more than a factor of 2, from about 12×10^6 m^3 s^{-1} in the southwestern Weddell to about 28×10^6 m^3 s^{-1} farther north. The increase in northward transport was compensated for by westward flow from the interior of the gyre into the western boundary region. About 5–6 $\times 10^6$ m^3 s^{-1} of the northward transport was contained in a 300–500 m thick bottom layer of cold water. This layer, whose transport increased by about 1×10^6 m^3 s^{-1} from south to north, was identifiable by its water mass characteristics as Weddell Sea Bottom Water originating on the southwestern and western shelf regions. Its north flowing volume was consistent with past estimates of a 1.5–2 $\times 10^6$ m^3 s^{-1} production rate coupled with a 300–400% transport increase due to entrainment during downslope flow from the shelves to the deep basin. The maximum (northernmost) northward transport, less the bottom water transport, is consistent with previous estimates for wind-driven transport in the Weddell Gyre provided that bottom friction and the sea ice influence on wind forcing are taken into consideration.

1. Introduction

Circulation in the western Weddell Sea is dominated by a northward flowing current which is the western limb of a primarily wind-driven, cyclonic gyre [*Gordon et al.*, 1978; *Deacon*, 1979; *Gordon et al.*, 1981; *Orsi et al.*, 1993]. This northward flow serves as the primary egress of water from the Weddell Sea, which is a major site of ocean water modification and deep water formation, to the remainder of the World Ocean.

Circulation in the Weddell Sea has proven difficult to quantify. Geopotential surface heights above the 1000-dB level, computed using historical data, show only very weak surface currents [*Gordon et al.*, 1978]. Similar computations carried out using more closely spaced data obtained from the northwestern Weddell Sea during March 1986 also showed small currents [*Nelson et al.*, 1989]. *Carmack and Foster* [1975] used short-term current measurements as a basis for deriving a total Weddell Gyre transport of 97×10^6 m^3 s^{-1}. Closure of the gyre circulation, which was assumed to be driven by Sverdrup transport, was postulated by *Gordon et al.* [1981] to require a western boundary current along the Antarctic Peninsula with a maximum northward transport of about 76×10^6 m^3 s^{-1}, vertically integrated current speeds of about 8 cm s^{-1} and a width of about 225 km at 65°S. *Limbert et al.* [1989] report, however, lower net ice drift speeds of 4–5 cm s^{-1} well within *Gordon et al.*'s [1981] hypothetical western boundary current.

The Weddell Sea is a major site for deep water formation [*Deacon*, 1933; *Gordon et al.*, 1993]. Thus, in addition to a wind-driven gyre component of the boundary current, we would expect to see a deeper circulation whose dynamics and transports reflect an input of dense water in the southern and southwestern Weddell Sea. Past field data have been inadequate to resolve uncertainties in upper layer current speeds, to quantify the volume transports associated with this western boundary region, or to determine internal and deep structures which might be associated with the western boundary current or with deep convective circulation along the western boundary.

During early austral winter (late February to early June) 1992 a joint U.S.-Russian manned ice station named Ice Station Weddell 1 (ISW-1) drifted northward in the western Weddell Sea from 71.5°S to 66°S along about 53.5°W [*Ice Station Weddell Group*, 1993]. Temperature and salinity data were obtained along the track of this drift and along four

[1]Formerly at Science Applications International Corporation, Bellevue, Washington.

Paper number 95JC00965.
0148-0227/95JC-00965$05.00

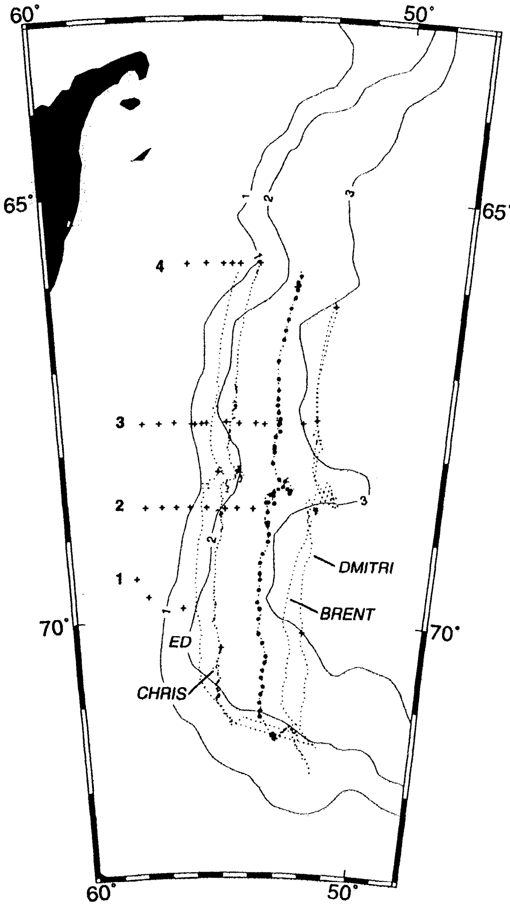

Figure 1. Geographical location of the austral winter 1992 Ice Station Weddell 1 (ISW-1) drift experiment. Large dots show locations of CTD casts along the manned station drift track, while plus signs show casts made along zonal transects 1–4 using a helicopter based at the manned camp. Dotted lines labeled Ed, Chris, and Dimitri show trajectories of the three remote, drifting current meter arrays. A fourth array, "Brent," was not equipped with current meters.

zonal cross-slope transects (Figure 1). Currents were measured at the manned drifting station and at three additional, remotely located sites (Figure 1). This paper describes and discusses our analyses of these data, emphasizing circulation and transport processes.

2. Data Collection and Processing

2.1. The Field Program

The data reported here were acquired from the northward drifting sea ice pack of the western Weddell Sea during the period from February 26 to June 3, 1992. Temperature and conductivity data were obtained on at least a daily basis from the manned ice camp ISW-1 using a Neil Brown conductivity/temperature/depth (CTD) profiler, providing a closely spaced meridional transect extending from 71.5° to 66° south latitude along approximately 53.5° west longitude (Figure 1). Temperature and conductivity data were also obtained along four zonal transects using a helicopter-borne Seabird CTD (Figure 1). These zonal transects extended from the continental shelf eastward onto the continental rise where water depths exceeded 3000 m, providing coverage of the continental slope region.

Currents were measured throughout the program using Neil Brown smart acoustic current meters (SACMs) which were suspended through the ice at four sites. These sites were arrayed along a zonal transect which was about 150 km long and which passed through the manned ice station, with one site being situated at the manned station. Each site drifted northward with the pack ice, so that currents were measured within a meridional swath about 150 km wide (Figure 1), although failure of the easternmost current array reduced the swath width to 80–90 km during the second half of the program. The current meters were suspended from the ice at depths of 50 and 200 m. Some units malfunctioned, so that data were not obtained from both depths at all sites (Table 1). Geographical position of the manned site was measured using a GPS navigation system. Positions of the unmanned sites were measured using Metocean ice buoys which utilize Service Argos to provide satellite-derived records of positions.

2.2. The Data Processing

The CTDs used for both the helicopter and base camp data acquisition were calibrated prior to and following the field work. Additional salinity calibrations were carried out during the field program by comparing CTD-derived salinities with those obtained through analyses, carried out at the ice camp, of water bottle samples. Finally, the data were used to construct 4-m vertically averaged bins with accuracies of 0.005°C and 0.005 psu (where psu is defined as practical salinity unit, and 1 psu = 1 ppt salt by weight) in temperature

Table 1. Depths, Start and End Dates of the Time Series Current Records Obtained From Each of the Drifting Sites

Record Dates*	Ed		Chris		ISW		Dimitri	
	50 m	200 m	50 m	200 m	50 m	200 m	50 m	200 m
	...	...	...	...	50–62	50–62	...	...
	65–110	...	52–101	...	...	...	78–102	63–102
					67–150	67–150		
	118–147	...	113–148	113–148			...	...

*Record dates are in Julian days.

Multiple segments at some sites reflect recovery/redeployment of the current meters. Differing start or end dates at different depths for the same site reflect problems which were encountered with some of the current meters.

and salinity, respectively. These were used subsequently to compute the field of density and the dynamic topography.

The current data were obtained using instruments which drifted northward along with the pack ice and therefore documented the relative ice-water motion. Correction for the ice motion was necessary to obtain the true currents and was done as follows. The geographical positions of the drifting current meter arrays, obtained using Argos buoys, were used to compute drift velocities, which were in turn smoothed with the complex demodulation routine of *McPhee* [1988]. This routine is intended to minimize those errors resulting from the position estimates (about 100 m per fix) by assuming that the ice moves in response only to winds and to tidal and inertial currents. The measured current velocities were corrected to absolute currents by subtracting the derived ice velocities. The measured current data, uncorrected for drift, is assumed to have the manufacturer's specified instrumental accuracy of 1 cm s^{-1}. Given that we obtained about 20 location fixes per day, and the largest position error following application of *McPhee*'s [1988] filter is about 100 m, the worst case drift speed error would be about 2.5 cm s^{-1}. In the worst case the instrumental and drift speed errors would be additive and would lead to an error in true current speed of about 3.5 cm s^{-1}. We have no reason to suspect that the position errors were maximal, nor any reason to suspect they were other than random.

An additional check on the current measurements was done by running sequential, overlapping 15-day tidal analyses on each record using the method of *Foreman* [1978]. These analyses supplied sequential values of four major component amplitudes and phases which were sufficiently statistically significant, based on error estimates output along with the amplitude and phase information, to verify the time bases and provide an additional rough check on the recorded current speeds. These tidal analyses verified that, while the measurement sites drifted northward, variations in the tidal parameters were small and regular [see *Levine et al.*, also manuscript in preparation, 1995], so that regional changes in these parameters did not significantly inhibit their use as a time base check. The sequential tidal analyses used to validate the current data showed amplitudes for individual constituents varying by well under 1 cm s^{-1} between the sequential datasets used for the computations.

Since this paper focusses on subtidal current components, the true currents resulting from the foregoing manipulations were filtered using a 40-hour low-pass filter which would have smoothed out much of any random error. The validity checks described above lead us to believe that the low-pass filtered data used for the below analyses are accurate to better than 1 cm s^{-1}. The resulting currents are shown plotted as functions of latitude for each of the drifting sites (Figure 2) and as vectors, derived by applying a spline fit to the 40-hour low-pass filtered data and subsampling daily, plotted along each of the drift tracks (Figure 3).

3. Results

3.1. Thermohaline Stratification

A sequence of CTD stations (Figure 1) obtained from the ice station revealed the thermohaline stratification typical of the rest of the Weddell Gyre (Figures 4 and 5): a cold, low salinity surface layer separated by a thin, weak pycnocline from a thick layer of relatively warm and salty water referred to as Weddell Deep Water (WDW), and a cold bottom layer [*Gordon et al.*, 1993] (Figure 4). Surface layer stratification was stronger early in the drift as late summer conditions lingered, but later in the drift (and in the season) the mixed layer more closely approached homogeneity [*Ice Station Weddell Group*, 1993]. The WDW maximum temperature and salinity core water is drawn from the Circumpolar Deep Water into the Weddell Gyre at its eastern margin near 30°E [*Orsi et al.*, 1993]. There are, however, some differences. In the western Weddell Sea the depth of the maximum temperature core of the WDW was about twice that at the Greenwich meridian [*Huber et al.*, 1989], or about 550 versus 250 m. The maximum temperature was somewhat deeper at the southern end of the ISW-1 drift, attaining greater than 800 m depths near 71.3°S. The salinity maximum averaged about 800 m in depth. Both of these core layers were slightly warmer and saltier, respectively, in the southern half of the section than farther north. The depth of the upper 0°C

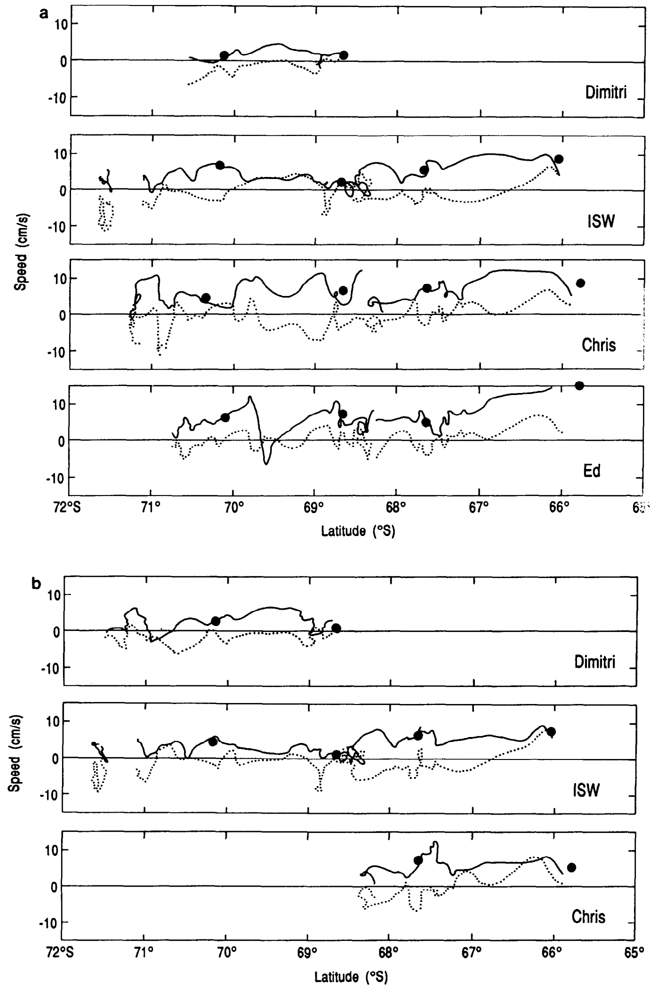

Figure 2. North (solid) and east (dotted) components of the 40-hour low-pass filtered (a) 50-m currents and (b) 200-m currents measured at four drifting arrays plotted as functions of latitude. Positive values are northward and eastward, respectively. Solid circles show the latitudes at which the drifting sites crossed zonal transects 1–4 and also indicate the mean northward currents which were used in transport computation (see text and Table 2). Occasional loops in the plots reflect brief periods of southward drift superimposed on the generally northward drift of the sites.

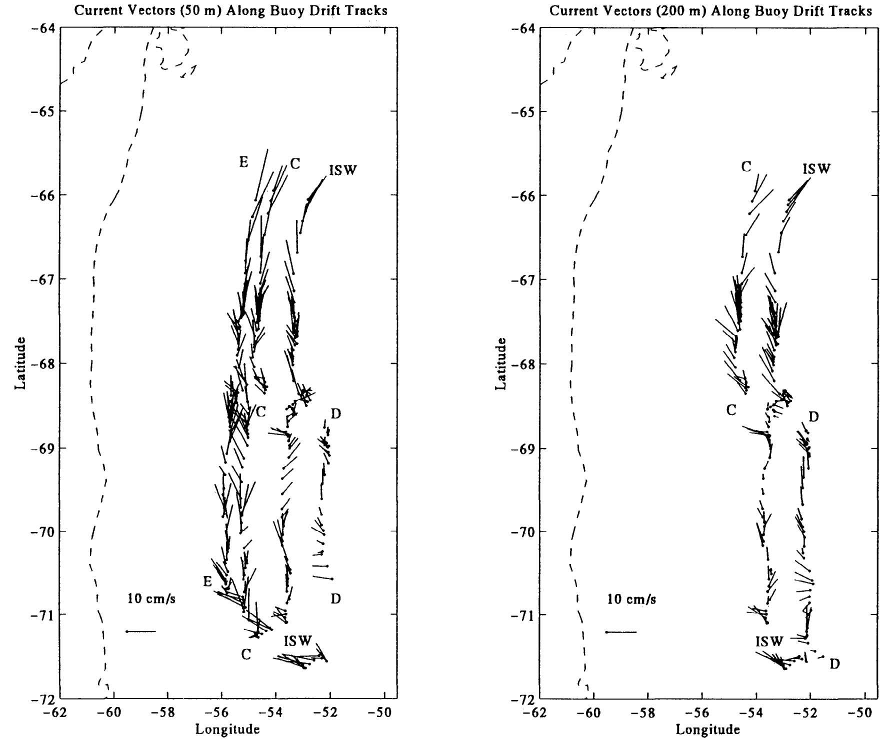

Figure 3. Daily mean (left) 50-m and (right) 200-m 40-hour low-pass filtered current vectors, subsampled daily, plotted along the drift tracks for the four current arrays. E indicates drifting site Ed, C indicates Chris, ISW is ISW-1, and D is Dimitri.

isotherm, located within the pycnocline, was also greater in the west or about 300 m as compared to 150 m farther east. Thus a greater proportion of cold upper layer water was present in the western boundary region than is typically encountered in the eastern Weddell.

Perhaps the most dramatic hydrographic feature in the western Weddell was a benthic layer having the temperature/salinity characteristics of Weddell Sea Bottom Water. This layer consisted of a thin (300–500 m) layer of very cold, low-salinity water which was also characterized by high dissolved oxygen concentrations [*Huber et al.*, 1994]. Helicopter sections 2 and 3 (Figure 1) revealed a thin, high-salinity (>34.6 psu) layer in contact with the continental slope; section 3 is presented as it was the more complete of these two sections (Figure 5). Cold, saline shelf water observed at the western ends of helicopter sections 1–3 (again, shown on section 3 in Figure 5) presumably was spreading into the deep ocean to advect northward as a part of the overall western boundary flow. The benthic layer thickened to the north near 66.1°S consistent with vertical entrainment and mixing [*Gordon et al.*, 1993], probably due in great part to the strong near-bottom currents discussed below.

Considerable hydrographic complexity was associated with a shelf break frontal zone. The surface layer and pycnocline deepened toward the west, with the upper (in the pycnocline) 0°C isotherm deepening to 400 m before folding downward into the deep water at the shelf break (Figure 5). Within a distance of only 20 km the temperature at 500 m decreased by more than 2°C from east to west, a temperature range equal to about 2/3 that encountered throughout the entire Weddell Gyre. The intense bottom boundary layer described above emanated from this shelf/slope frontal feature. The baroclinic currents at the front, discussed in detail below, were large and formed a jet along the shelf break. Water in contact with the continental slope was generally more saline than that within the middle part of the benthic layer, producing a minimum salinity layer several tens of meters off the seafloor. This feature can be traced to a trough in the isohalines which was centered just seaward of the shelf break and formed a ribbon of low salinity as manifested on a horizontal surface (and as discussed by *Gill* [1973]).

3.2. Measured Upper Layer Currents

The flow was generally northward throughout the study region, with peak speeds occurring in the northern part and particularly in the northwest where daily mean 50-m speeds exceeded 10 cm s^{-1} (Figures 2 and 3). An exception occurred at about 68°30′S when, for a period, currents were generally weak and variable. Considerable variability was present in zonal flow throughout the drift, and this variability was not always well correlated between the different sites. Similarly, 50-m zonal flow was not always correlated with that at 200 m. As an example of this, the 50-m currents diverged horizontally in the east-west direction from about 70°–69°S between drifting sites ISW and Chris (Figure 3). A weak zonal convergence was present between sites Chris and ISW at both 50- and 200-m depths centered on about 67°S. Just south of this convergent region, and north of the region where circulation was sluggish, significant westward flow occurred at 200 m. Zonal flow at 50 m was variable in this region except at ISW where westward flow was present but was weaker than at 200 m.

The 50- and 200-m currents were in closest agreement at the northern and southern ends of the drift tracks and also had

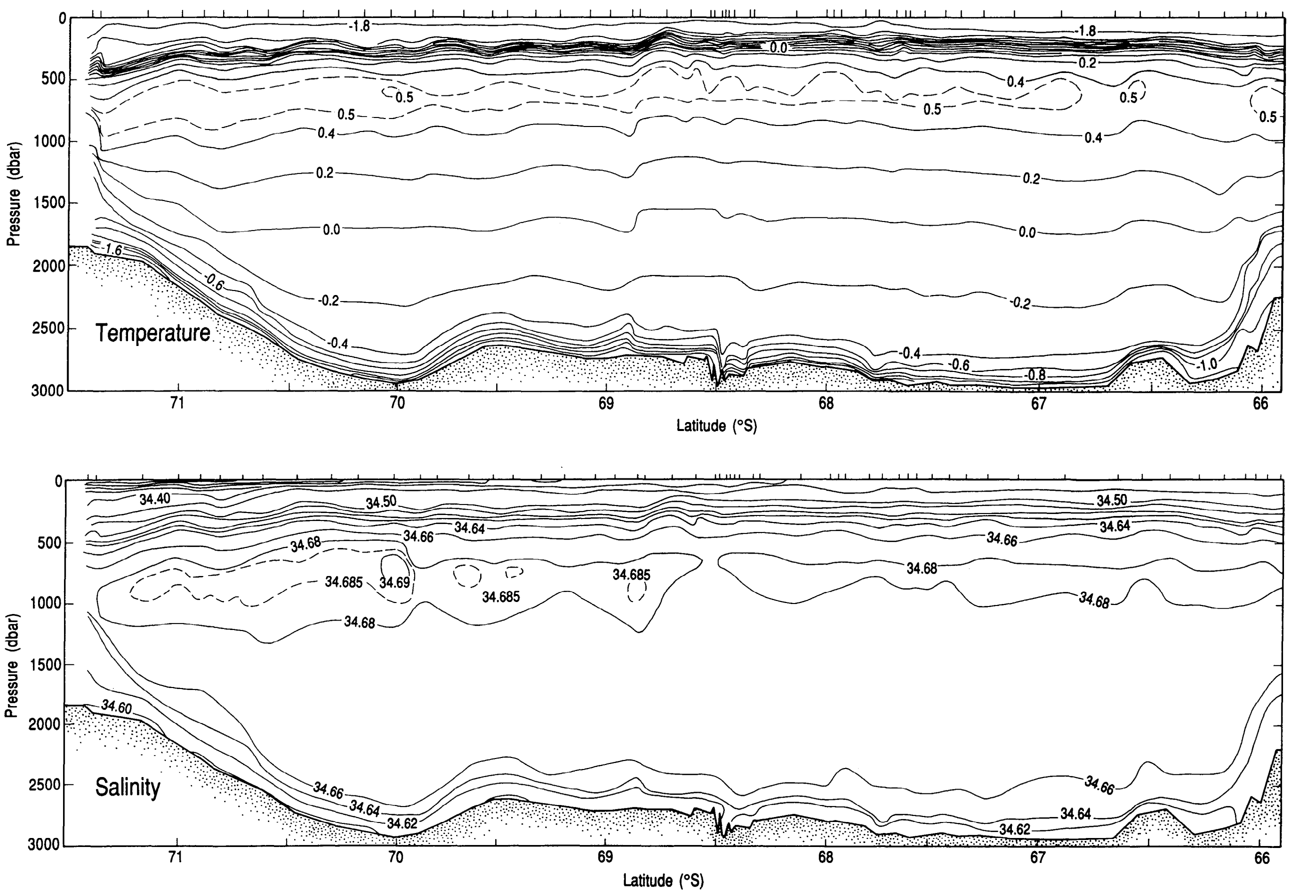

Figure 4. Distribution of (upper) potential temperature Θ and (lower) salinity S along the ISW-1 drift track. Contour intervals are 0.2°C and 0.02 psu in Θ and S, respectively, except where indicated otherwise by use of dashed, labeled contours.

higher speeds than elsewhere. At the south end, currents were more westward than northward. At the north end significant, but smaller, eastward components were present. Reference to the topography (Figure 1) suggests that currents at the north and south ends of the drift tracks were strongly topographically controlled. The higher-speed currents paralleling the bottom topography at these locations probably represent the eastern edge of the high-speed core of the barotropic western boundary flow along the continental slope. A significant baroclinic contribution to this speed may also be present close to the shelf break, as discussed in the following section.

3.3. Estimated Deep Currents

Before computing volume transports, we extrapolate the observed 50- and 200-m currents throughout the water column by first computing the baroclinic geostrophic currents normal to each of the four zonal helicopter CTD transects and the meridional CTD transect constructed along the manned ice camp drift track. These computed values are then adjusted using the measured currents in order to yield an estimate of the total (barotropic plus baroclinic) currents throughout the water column. There is no need to postulate a level of no motion because we have adjusted our computed values to known currents at specified depths.

Use of the drifting current meter data to adjust the computed geostrophic currents was not straightforward. The current records show significant subtidal variability which reflects both time changes and spatial variability as the array drifted northward (Figures 2 and 3). Current speeds for adjustment of the computed baroclinic profiles were estimated in the following way, in an attempt to minimize possible error while at the same time recognizing that some error is inherent due to the data having been collected from moving platforms.

The current records from 200 m were selected as the primary data set for adjusting the computed geostrophic baroclinic currents because they are less likely to reflect the effects of surface winds and ice motion than the shallower 50-m records. The 50-m data were used, when available, to compare measured with computed (baroclinic geostrophic) shear between the 50- and 200-m levels. Where only the 50-m data were available these were used instead of 200-m data, in some instances after applying a correction for vertical shear as discussed below, to adjust the computed baroclinic currents.

Each of the 50- and 200-m current records was used initially to compute an integral time scale (defined, for example, as in the work by *Monin and Yaglom* [1971]). The two longest records, those from 50 and 200 m at site ISW, yielded about a 5- to 6-day scale. This timescale is consistent with the periods derived through visual inspection of the time series current plots, and we accept this value as a reasonable indicator of the time scale for variability.

For a fixed mooring, averaging over several timescales is desirable in order to obtain a statistically significant mean. In

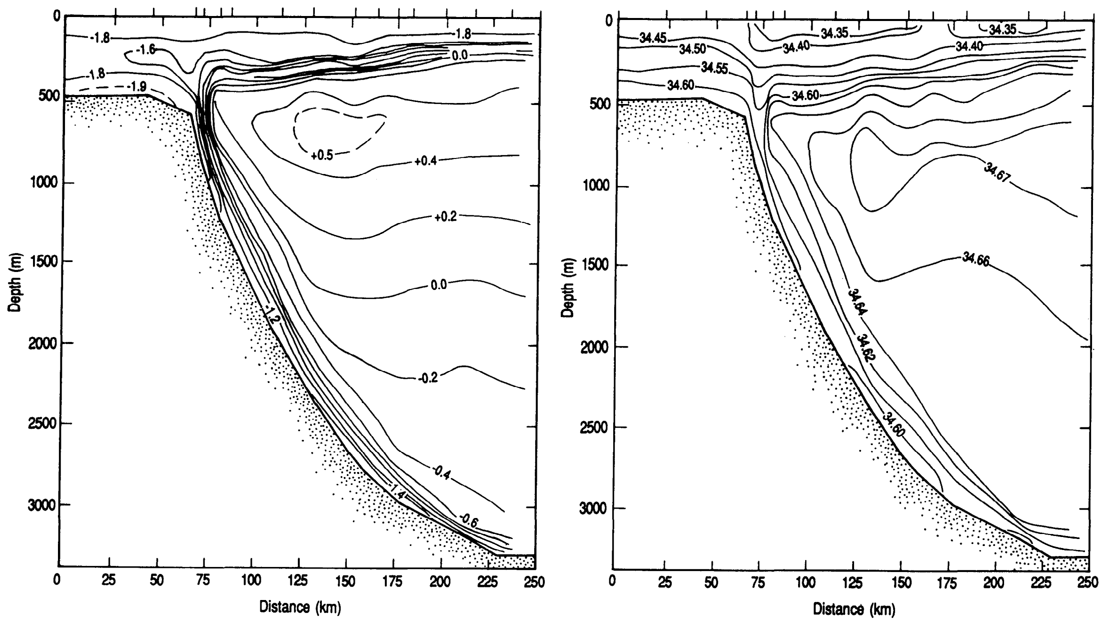

Figure 5. Distribution of (left) potential temperature Θ and (right) salinity S along helicopter section 3, which was the most complete of the four zonal transects occupied by helicopter based at the ISW-1 camp. Contour intervals are 0.2°C and 0.02 psu for Θ and S, respectively, except where indicated otherwise by use of dashed, labeled contours.

our case in which the moorings traverse significant distances over time, however, averaging over several integral timescales would incorporate measurements over a large enough zonal extent that geographical variations could become a significant factor in the variability. The following compromise was made.

In the case of each of the four zonal transects, means and standard deviations for the northward (v) currents were computed from the 50 and 200 m current records in two ways. First, the computations were carried out over 10-day windows centered on the times when each of the four zonal CTD transects intersected each of the mooring drift tracks. Second, they were carried out over a meridional spatial window spanning 0.5° latitude and centered on the latitudes at which each CTD transect intersected each mooring drift track. Given an overall mean northward drift speed for the moorings of about 5 cm s^{-1}, these two methods yield roughly the same number of overall data points for each computation. The averaging intervals were truncated at the northern ends of the drift tracks where current data were acquired for only about the first half of these temporal and spatial intervals. Eastward current components were computed similarly but only at only those locations where an eastward flow component would have contributed to the cross-transect transport (i.e., all of transect 1 and the eastern half of transect 4). The results of these current computations are presented in Table 2. In general, values computed using the two different modes of averaging at each location agreed with each other to within the standard deviations, providing confidence that we have indeed derived representative values. Because for purposes of volume transport computation the transects are defined in space, as compared to time, we select the 0.5° meridional spatial averages and standard deviations for derivation of total currents from the computed geostrophic currents.

Temperature and salinity data from the four zonal transects were used to compute the baroclinic geostrophic current profile between each station pair relative to the sea surface. Each computed current profile was adjusted using a speed offset derived from the current measurements such that the 200-m speed (or in some cases the 50-m speed if there were no current measurements available from 200 m) agreed with the measured current. Values of measured speed for these adjustments were derived for each location by linearly interpolating the current values between the drifting sites. At some locations, this interpolation likely provided a good estimate, whereas in other places some error may have been incurred. Perusal of the current speed at each measured comparison point (Table 2) provides a rough estimate of its validity which will be discussed further below. Errors in the measured temperature and conductivity and in the geographical locations of the data points can contribute to errors in the computed baroclinic currents. Because of the care used in obtaining the T and S data and the known accurate GPS positioning used to obtain site locations, we assume that these errors were negligible relative to those possibly generated by derivation or interpolation of the measured currents used to correct the baroclinic currents to a known reference level. Errors may also arise from density changes in the water column during occupation of the CTD transects. This may have been a factor, in particular, for the very closely spaced stations over the upper shelf break on transect 3.

No current data measurements for the zonal transects extended west past the upper continental slope, and those for transects 3 and 4 did not extend east to the ends of the transects. Current speeds at 50-m depths west of the westernmost current meters (site Ed) were assumed to remain constant and equal to the values measured at Ed. The 50-m/200-m shear at ISW (for the first half of the drift) or Chris (for the second half of the drift) was used to adjust the 50-m currents at Ed for vertical shear. These "shear-corrected" 50-m currents were then used to correct the

Table 2. Current Statistics Computed for Use in Estimating the Volume Transports, Listed for Each Intersect Between a Drifting Current Measurement Site (Horizontally) and Zonal Transects 1–4 (Vertically)

	Ed			Chris			ISW			Dimitri		
	v	u	n	v	u	n	v	u	n	v	u	n
				Transect 1								
Latitude interval for 50 m	6.3±0.4	0.4±1.4	124	4.1±1.3	0.0±1.4	136	6.5±0.7		116	1.2±1.4		149
Latitude interval for 200 m	···	···	···	···	···	···	4.6±1.1		116	3.1±1.0		149
Time interval for 50 m	6.7±3.0	−0.2±1.7	240	5.1±2.4	0.3±1.6	240	5.1±1.7		240	1.4±1.4		216
Time interval for 200 m	···	···	···	···	···	···	3.6±1.7		240	3.2±1.0		240
				Transect 2								
Latitude interval for 50 m	6.7±2.1		269	6.2±2.8		262	1.8±1.7		479	1.7±0.7		85
Latitude interval for 200 m	···	···	···	···	···	···	1.2±1.3		479	1.0±1.3		83
Time interval for 50 m	5.7±1.6		240	5.4±2.4		186	1.0±1.4		240	1.5±0.8		108
Time interval for 200 m	···	···	···	···	···	···	1.2±1.0		240	0.4±1.4		106
				Transect 3								
Latitude interval for 50 m	4.9±2.3		308	6.8±1.7		335	5.3±1.6		388	···	···	···
Latitude interval for 200 m	···	···	···	7.6±3.3		335	6.4±1.4		388	···	···	···
Time interval for 50 m	4.6±2.5		240	7.4±1.3		240	4.1±0.8		240	···	···	···
Time interval for 200 m	···	···	···	8.0±3.3		334	5.8±1.3		240	···	···	···
				Transect 4								
Latitude interval for 50 m	15.5±0.9		40	8.3±1.4		32	8.4±1.6	5.5±0.8	81			
Latitude interval for 200 m	···	···	···	5.8±1.3		31	7.6±1.2	5.0±0.9	81	···	···	···
Time interval for 50 m	13.6±1.7		120	10.3±1.9		80	8.5±1.3	4.3±1.8	124	···	···	···
Time interval for 200 m	···	···	···	6.9±1.3		79	6.8±1.5	3.3±0.9	124	···	···	···

Values are given as mean v (positive north) ± standard deviation, mean u (positive east) ± standard deviation and n, the number of hourly data points used for the computation. Note that u was computed only where it was needed where transects 1 and 4 departed significantly from zonal orientation. Values are shown as computed over latitude intervals and over time intervals as described in the text, for 50- and 200-m depths. Center dots indicate that no measurements were obtained.

computed geostrophic currents. The easternmost currents on transect 3 and 4 were corrected using currents extrapolated linearly from Chris and ISW. All of these extrapolations were done as "working assumptions" and no other justification is claimed. Possible errors relevant to the volume transport computation for transect 3 will be discussed below. The resulting vertical distributions of current normal to each transect are shown in Figure 6.

The vertical distributions of currents reflect imposition of the measured northward flow at 50 and 200 m. Northward flow seaward of about the 1000 m isobath decreased initially with increasing depth to a minimum typically about 500 m above the seafloor. Below this minimum, northward current speeds increased sharply toward the seafloor so that the highest northward current speeds in the entire profile occurred near the seafloor. These deep northward flows were strongest at or just seaward of the shelf break. This distribution is seen particularly dramatically, subject to some possible error inherent in westward extrapolation of the 50-m current speeds, on transect 3 where corrected northward near-bottom speeds exceeded 40 cm s^{-1}.

Computation of zonal currents through the essentially meridional ISW drift track was approached somewhat differently than for currents through the zonal transects, because the ISW CTD casts were closely spaced compared to those on the zonal transects, and currents were continuously measured along the track. Rather than using every CTD cast along the northward drift track, casts spaced at approximately 0.5° latitude intervals were used for computed baroclinic geostrophic current speeds normal to the transect (i.e., zonal currents, to a good approximation except very early in the drift). This spacing was compatible with the 0.5° latitude and 10-day intervals used in computing the currents for the zonal transects. The measured zonal currents along the ISW drift track were passed through a spline fit and subsampled at locations coincident with sites where baroclinic currents had been computed. The computed currents were then adjusted, as for the zonal transects, using the spline fit 200-m currents to yield the vertical distribution of zonal flow along the drift track (Figure 7).

Upper layer currents across the meridional drift were generally small and were dominated by the 200-m measured currents used to adjust the computed baroclinic currents. The distributions of current speed clearly show, near the southern and northern ends of the transect, the enhanced flow over the continental slope which reflects the northward regional boundary flow. Current speeds in this flow, which was present throughout the water column in bottom depths less than about 2500 m, were 6–7 cm s^{-1} and did not vary greatly with depth although some bottom intensification, particularly near the north end of the transect, reflected the baroclinic effect of the dense plume of bottom water described above. Elsewhere, particularly from about 69° to 70°S, current speeds were lower. The westward flow observed from about 67° to 69°S in the measured currents is clearly evident, with 2–3 cm s^{-1} speeds typical for most of the water column but with some increase toward the bottom.

Several features which appeared on the basis of their spatial extent to be mesoscale were evident along the meridional transect, which was sampled much more densely than the zonal transects. Our sampling was however inadequate to define these features, which are mentioned here only in order to document their presence. Neither their spatial scales nor associated currents suggest that they significantly impacted the regional processes which are the primary focus for this work.

The benthic layer deepened abruptly just north of 66.5°S.

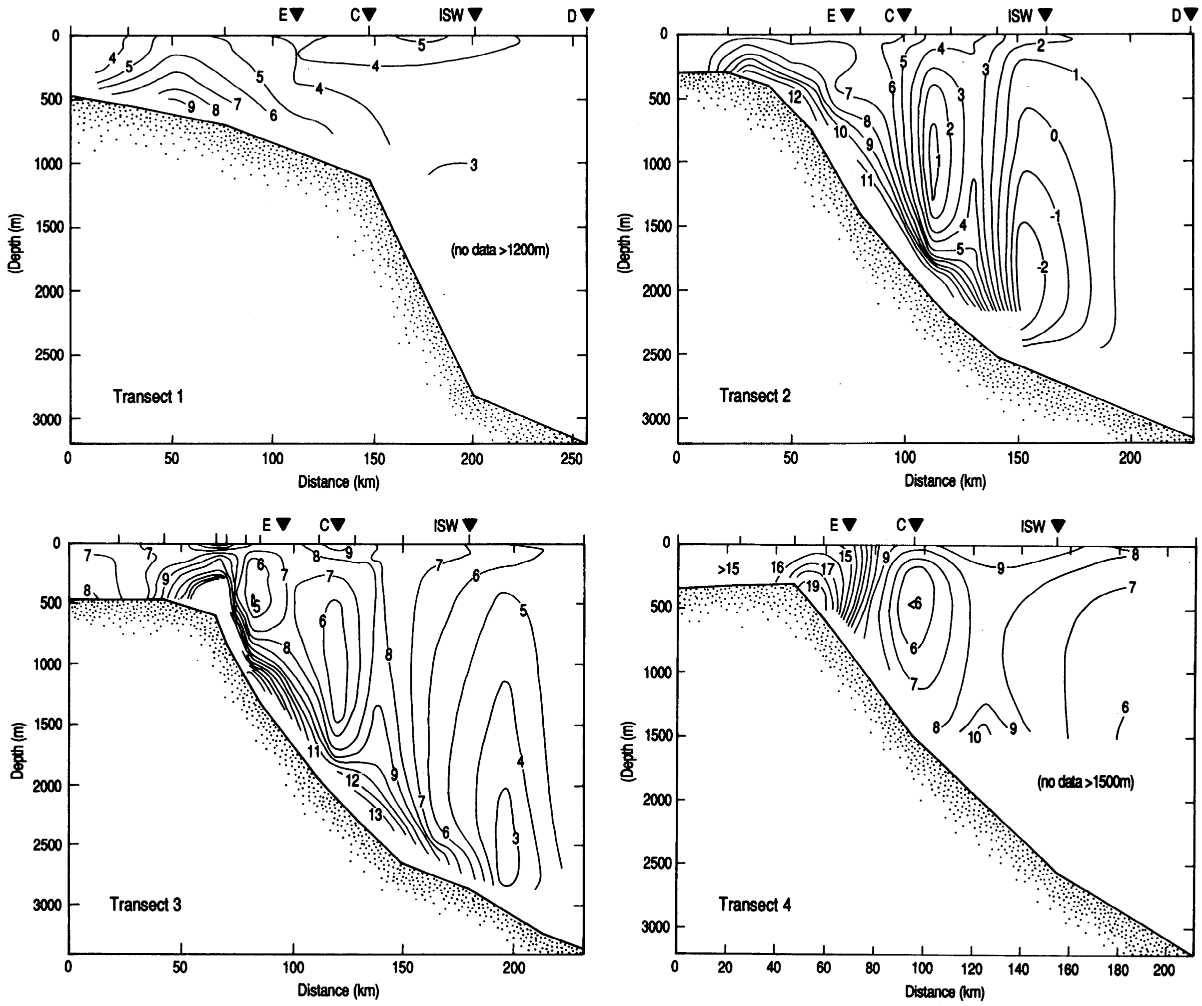

Figure 6. Distribution of current speeds in centimeters per second normal to zonal transects 1–4. Positive values indicate northward flow. Arrowheads above the top axis indicate locations where the transect intersected drifting current meter arrays Ed (C), Chris (C), ISW, and Dimitri (D). Currents are referenced to measurements obtained from either 50 m or from 200 m at each of the drifting current meter arrays, as discussed in the text. Note that the horizontal current structures rely upon considerable interpolation and extrapolation as discussed in the text, whereas more confidence can be placed in the vertical structures which are based on dynamic computations.

The currents show stronger near-bottom baroclinic flow directed westward in this area (Figure 7). Weakening of the benthic layer is consistent with intrusion of bottom water into the boundary region from the gyre interior. The increased eastward geostrophic flow, with associated strong bottom currents, suggests that strong egress of water from the continental margin, with enhanced bottom stress-related mixing, was occurring.

3.4. Volume Transport Estimates

Volume transports were computed normal to zonal transects 2 and 3 and normal to the meridional transect defined by the ISW drift track by vertically integrating the computed total speeds (Figures 8 and 9). Transports were not derived for zonal sections 1 and 4; in view of the significant deep current structure evident on sections 2 and 3, it was judged that the lack of deep CTD data on transects 1 and 4 could have led to significant, and impossible to estimate, errors in computed transport.

While transport computation normal to the meridional transect was straightforward due to the regular and relatively tight station spacing, some assumptions were needed in computing transports normal to transects 2 and 3 where these intersected the continental slope. Transports could be derived through vertical integration of computed speeds only to the depth where the shallowest station of a given pair intersected the seafloor, so that near-bottom data gaps remained after integration. Transports through these gaps, triangular in the vertical plane of the transect and bounded by the seafloor, were estimated by multiplying the cross-sectional area of each gap by a current speed normal to the gap. This normal current speed was estimated by interpolating the adjacent (upslope and downslope) computed current speeds into the gap. Since the computed near-bottom speeds did not vary radically with depth (see Figures 6 and 7), we believe that this method contributed minimal, if difficult to ascertain, error to the overall vertically integrated transports.

Errors in the transports normal to the meridional section

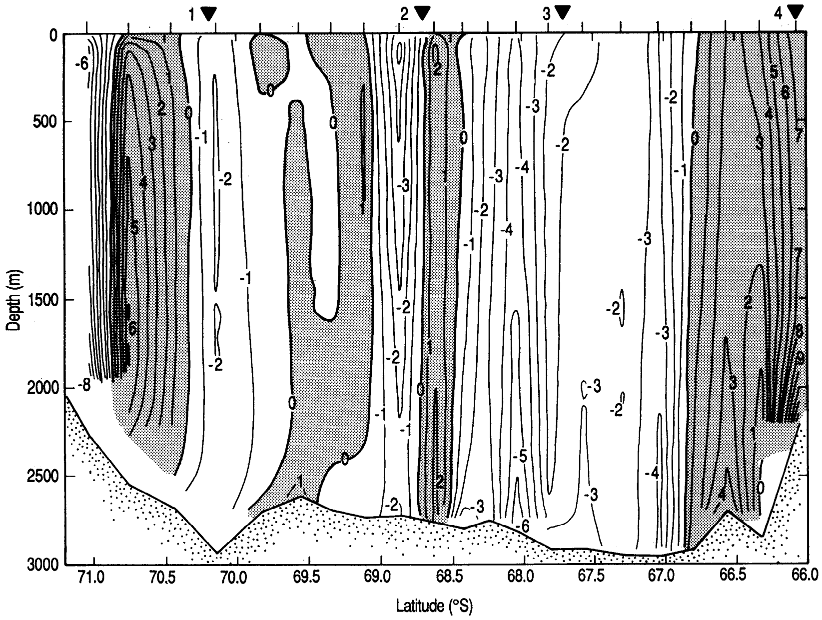

Figure 7. Distribution of current speed in centimeters per second normal to the meridional transect described by the northward drift of manned ice camp ISW-1. Positive values (shaded) indicate eastward flow. Numbered arrowheads along the top axis indicate locations where the transect intersected zonal CTD transects 1–4. Currents are referenced to measurements obtained from 50 and 200 m depths at the drifting current meter sites, as discussed in the text.

were computed for each CTD station pair using the standard deviations in the measured current speeds appropriate to that station pair. Errors in computed transport due to temperature, salinity or station position were assumed negligible relative to those due to the current variability. The resulting transports are shown in Figure 8.

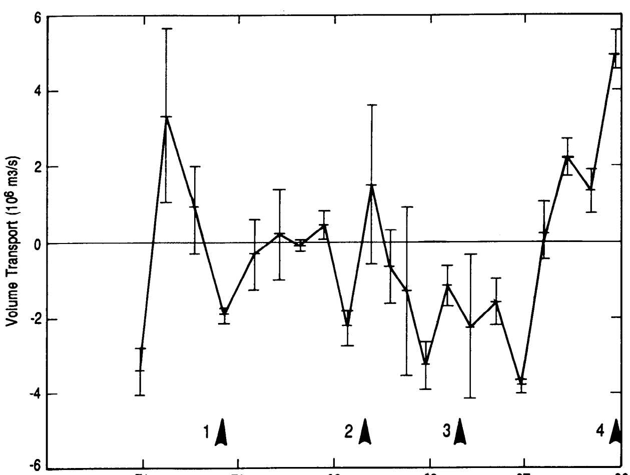

Figure 8. Distribution of vertically integrated volume transport in 10^6 m^3 s^{-1} for each station pair normal to the meridional transect plotted by station pair as a function of latitude. Positive values indicate eastward transport. Error bars are based on standard deviations of the current speeds used in estimating the transports. Numbered arrows along the lower axis show the locations where the meridional transect intersected zonal transects 1–4. Underlying bottom depths are shown on Figure 7.

Errors in the transports through zonal transects 2 and 3 due to measured current fluctuations were likewise estimated by applying the standard deviations for the measured currents to the transport estimates for each CTD station pair (cf. Table 2). Possible errors due to zonal interpolation or extrapolation of data, as noted above, cannot be reasonably estimated. Errors incurred by westward extrapolation of the measured currents over the continental shelf break and shelf

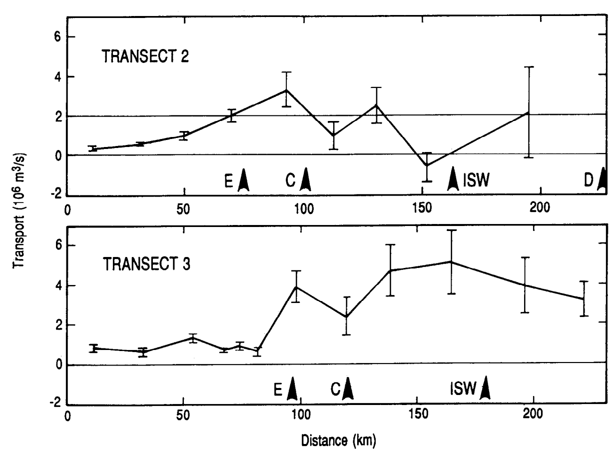

Figure 9. Distribution of vertically integrated volume transport in 10^6 m^3 s^{-1} for each station pair normal to zonal transects 2 and 3 and plotted by station pair as a function of distance from the westernmost CTD station (east being to the right). Positive values indicate northward transport. Error bars are based on standard deviations of the current speeds used in estimating the transports. Arrowheads along the distance axes show the locations where the transects intersected the drifting current mooring sites. Underlying bottom depths are shown on Figure 4.

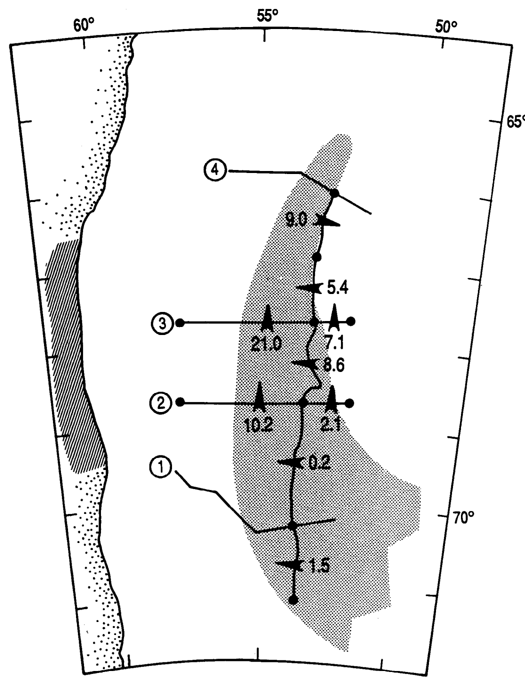

Figure 10. Vertically integrated volume transports, in 10^6 m^3 s^{-1}, normal to selected transect segments whose endpoints are defined by solid circles. Circled numbers identify the zonal transects, and arrowheads indicate flow direction. Hatched region on the Antarctic Peninsula indicates approximate location of the Larson Ice Shelf. Errors associated with the indicated transports can be derived from Figures 8 and 9 and from the text. Tongue-shaped, shaded area indicates the region within which $T_{max} > 0.5°C$.

are, however, limited because of the shallow water depths. The absence of current measurements at the eastern end of transect 3 poses a more serious potential problem as the order 3000 m bottom depths would lead to significant transport errors given errors in the estimated velocities. Computed transports through zonal transects 2 and 3 are shown, with error bars, in Figure 9.

Major features of the vertically integrated volume transports are summarized on Figure 10. Consistent with the measured currents, net meridional transport was northward. That through transect 2, which was the best documented transect in terms of upper layer current observations, was 12.3 (± 6.2) × 10^6 m^3 s^{-1}. That through transect 3 farther north was more than twice as great at 28.3 (± 8.1) × 10^6 m^3 s^{-1}. The errors given here are worst case, assuming that all individual station pair errors are of the same sign, and are subject to the above caveats concerning interpolation or extrapolation of measured current data. The transport was more than twice as large at transect 3 as at transect 2, and fluctuations in the measured currents were less as reflected in the relatively smaller (less than one third, as compared to one half) error at transect 3 as compared to transect 2. Most of the increased northward transport between these transects west of the meridional transect described by the ISW drift can be accounted for by westward transport of 8.6 × 10^6 m^3 s^{-1} across the meridional transect. The increase in northward transport by about 5 × 10^6 m^3 s^{-1} between transects 2 and 3 through the portions of those transects east of the ISW drift track is likely due as well to inflow from the east which continues to be large up to about the halfway point between transects 3 and 4, at which point it reverses to an eastward flow.

The meridional transect shows westward and eastward transport at its southern and northern ends, respectively, where it crossed isobaths and transected the flow paralleling isobaths on the western boundary. The westward transport of 1.5 × 10^6 m^3 s^{-1} shown south of zonal transect 1 reflects the influence of the eastward current discussed above and shown on Figure 7. The eastward transport associated with this current, computed using the same methods described above and all CTD data for its extent along the meridional transect, was about 4 × 10^6 m^3 s^{-1}.

The highest maximum temperature values (>0°C) were found just west of the ISW drift track, consistent with a marked spreading along the continental margin [*Gordon et al.*, 1993]. The currents along this spreading axis show a strong barotropic current at the more concentrated WDW core, and this current may contribute to its perseverance.

The high-speed near-bottom flow (Figures 6 and 7) reflects the northward flowing plume of cold, brine enriched water formed on the shelf regions to the south and west [*Gordon et al.*, 1993]. It is possible to estimate the volume transport of this flow. The thickness of the layer can be estimated by noting the distance above the seafloor at which the northward currents begin to increase with depth. For both transects 2 and 3 the layer thickness was nearly 500 m midway down the continental slope and decreased westward to perhaps 300 m at the shelf break. We assume a "typical" thickness of 400 m. Mean current speeds were impossible to compute because no values were available near the sloping bottom. For purposes of estimation, we simply take a rough horizontal mean of the highest computed near-bottom speeds, which were in fact about midway through the bottom layer. A speed of 11 cm s^{-1} was chosen representative for transect 2, while a somewhat higher value of 13 cm s^{-1} was used for transect 3. For comparison purposes, *Fahrbach et al.* [1994] report a near-bottom along-isobath mean current speed of about 11 cm s^{-1} at 1000 m depth near 63°S off Joinville Island. Their current speeds were computed using 1989–1991 data. *Nowlin and Zenk* [1988] report presence of a westward flow in southern Drake Passage which, they state, originated as the northward flowing bottom flow from the western Weddell margin. They report current speeds associated with this westward flow of 10–20 cm s^{-1}, which encompasses our assumed values. The current speeds we have selected yield transports for the 400-m-thick bottom layer of about 5.5 and 6.5 × 10^6 m^3 s^{-1} northward across transects 2 and 3, respectively, and suggest that the bottom flow comprises a significant fraction of the total northward transport.

4. Discussion

We have measured upper layer currents in the western Weddell Sea and have used these in conjunction with temperature and salinity data to compute volume transports in the northward flowing western boundary current of the Weddell Sea. We have defined a northward volume transport along the western boundary and have identified significant westward flow into the boundary region midway north along the boundary. Finally, we detected an extensive deep, northward flowing plume of dense water which contributed significantly to the overall northward transport. This section discusses these features.

We first approach, through comparison with some recent results, the question of whether or not our estimated transports are representative of climatological mean conditions. The only other solidly field-based estimates were made by *Fahrbach et al.* [1994], who obtained an extensive set of long-term current observations from taut-wire moorings deployed over three years across the Weddell Gyre from Kapp Norvegica (on the Antarctic coast near 12°W) to the northern end of the Antarctic Peninsula (cf. Figure 1). They used these observations to compute a time averaged gyre-wide transport of 29.5×10^6 m^3 s^{-1} with an estimated error of $\pm 9.5 \times 10^6$ m^3 s^{-1}. They assigned about 90% of this total, or 26.6×10^6 m^3 s^{-1}, to the boundary currents, which they defined as being within 500 km distance from the shelf break. Our maximum estimated northward volume transport at transect 3 of about 28×10^6 m^3 s^{-1} compares favorably with Fahrbach et al.'s results, though our transport estimates extend only about 200 km seaward of the shelf break rather than the 500 km by which they defined the boundaries.

The above field data-based estimates can be compared with earlier estimates which relied upon simple analytical models. *Gordon et al.* [1981] computed a wind-driven Sverdrup transport for the entire Weddell-Enderby Basin. They arrived at a maximum value for northward transport in the western boundary current of 76×10^{-6} m^3 s^{-1}, but noted that if basin-wide frictional effects were taken into consideration the western boundary transport dropped to a much smaller value of 46×10^6 m^3 s^{-1}. Their computations used, however, an open water air-sea drag coefficient for computing wind stress. Recent measurements carried out over the winter ice pack in the eastern Weddell Sea have revealed that presence of the ice cover reduces air-sea momentum transfer, at least in winter, by about one third [*Wamser and Martinson*, 1993; *Andreas et al.*, 1993]. Correcting the wind stress accordingly for presence of pack ice would have reduced *Gordon et al.*'s [1981] minimum (frictional) transport estimate for the western boundary. If the region were ice-covered year-round, transport would be reduced to about 30×10^6 m^3 s^{-1}, which is consistent with *Fahrbach et al.*'s [1994] results and with the greater of the two transports we report here through the zonal transects. The region is, however, only partially ice-covered from about January–May, the summer period [*Gloersen et al.*, 1992] which does not encompass the most severe winter storm events. The actual transport would be somewhat greater than if the region were ice-covered all year round. Further, about 6×10^6 m^3 s^{-1} of our computed transport of about 28×10^6 m^3 s^{-1} at transect 3 was due to the northward flowing bottom plume so that only about 22×10^6 m^3 s^{-1} are attributable to wind stress curl.

A westward transport of about 14×10^6 m^3 s^{-1} across the ISW drift track increased northward transport in the slope region between about 67°–69°S by more than a factor of 2. Since the ISW drift track coincided for much of its length with approximately the 3000 m isobath, only entering shallower depths near the start and finish of the drift, this transport crossed the 3000-m isobath where the slope is starting its gradual transition to the deep basin floor. The transport can thus be viewed as from the interior to the boundary region, and this is consistent with abrupt changes in depth of the isotherms and isohalines which were encountered at some locations. The isotherms changed depth between 68.8° and 68.9°S, shoaling northward at all depths shallower than 2300 m (Figure 4). The maximum salinity also appeared slightly lower to the north of about 68.9°S. At this latitude, the geostrophic flow across the ice station drift track reveals stronger baroclinic currents with a marked increase in westward transport (Figure 7). This flow pattern was consistent with the temperature-salinity property change, which suggests a westward shift of the WDW more typical of the interior portions of the gyre than of its western boundary, that is, shallower depths for the maximum temperature and salinity cores.

Water mass characteristics of the inflowing water were slightly different from those farther south, as exemplified by increased 200-m temperatures within and north of the region of westward flow (Figure 11). The corresponding 50-m temperatures show, in contrast, a northward decrease which was probably due primarily to combined seasonal cooling and mixed layer deepening (Figure 12).

The reason for the considerable westward transport which was present near the midway point along the ISW drift track is uncertain. The possibility that it was an isolated westward pulse seems ruled out by its broad spatial extent and lack of an apparent time-dependent forcing mechanism. Current data obtained from moored current meters farther north at about 63°S over the same time period and reported by *Fahrbach et al.* [1994] show no coincident increase in northward transport, as would be expected through volume continuity if a pulse-like flow event into the western boundary region occurred. A second possibility is that an existing flow was present all along the western boundary but was east of the region encompassed by our data south of about 68.5°S. A poorly documented, zonally oriented bottom ridge is present near 68.5°S in the vicinity where the westward flow was first observed. Although this feature was not particularly dramatic where it intersected the ISW drift track (see the bottom depths shown on Figure 7), it may have had greater relief elsewhere. Given the strongly barotropic nature of the flow field, relatively small topographic features have been observed to exert a strong influence over the currents elsewhere in the Weddell Sea [*Fahrbach et al.*, 1994]. This bathymetric control would contribute to westward flow in the region from about 67° to 69.5°S, more or less coincident with the meridional band where we observed westward flow.

Ice conditions appear consistent with a convergence zone in the region. Ice observations carried out during the 1992 program detected compression in the pack ice in the area of convergence formed between the westward flow and currents farther west which had no significant westward components (S. Ackley, CRREL, personal communication, 1993). This zone of ice convergence occupied the same area where Ernest Shackleton's vessel *Endurance* was crushed by the ice during its northward drift in 1915, which would be consistent with presence at that time of a westward flow such as reported above.

The northward flowing, near-bottom layer was a continuous and major feature along the continental slope from the shelf break to depths of more than 3000 m, and represents newly formed Weddell Bottom Water. Presence of this high-speed bottom flow was predicted for the western Weddell margin as early as 1969, based on bottom sediment samples [*Hollister and Elder*, 1969]. Two mechanisms have been proposed for formation of this water mass. *Foster and Carmack* [1976] utilized hydrographic data to hypothesize that shelf break mixing processes in the southern and south-

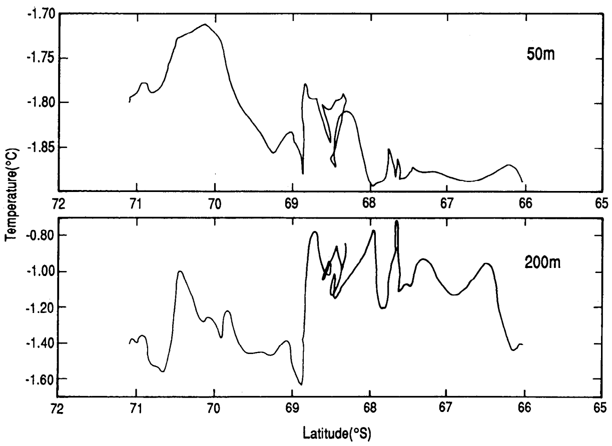

Figure 11. Temperature plotted as a function of latitude, obtained from the (upper) 50-m and (lower) 200-m deep current meters at the ISW-1 drifting site. As for Figure 2, loops reflect southward drift events.

western Weddell Sea were responsible for formation of bottom water, and estimate a Weddell Sea Bottom Water production rate of 3.6×10^6 m^3 s^{-1}. They note, however, that their production rate might vary from as small as 0.3 to as large as 30×10^6 m^3 s^{-1}. *Foldvik et al.* [1985] documented an outflow from beneath the Filchner Ice Shelf of cold, dense water as one source for this bottom layer. They used temperature, salinity and current data from the vicinity of the ice shelf to estimate an input of about 10^6 m^3 s^{-1} from beneath the shelf, and observed the resulting plume near 2500 m depth along the continental slope. This volume of outflow is not comparable with that of *Foster and Carmack* [1976], however. *Foldvik et al.*'s [1985] estimate was for the source water, whereas *Foster and Carmack*'s [1976] estimate was for the final bottom water. The new data cited in this paper have allowed *Gordon et al.* [1993] to identify, on the basis of water properties, the bottom plume covering much of the western Weddell Sea continental slope as a newly formed contribution to the Weddell Sea Bottom Water. *Gordon et al.* [1993] estimated a contribution from the shelf to the newly formed bottom water of less than 3×10^6 m^3 s^{-1}, which can be compared with our total northward transport in this layer through transects 2 and 3 of 5–6 $\times$ 10^6 m^3 s^{-1}, suggesting that 50% of the benthic layer transport is newly formed bottom water. The approximately 1×10^6 m^3 s^{-1} transport increase between transect 2 and transect 3 is consistent with a 1×10^6 m^3 s^{-1} growth per 100 km of continental margin of new inflow from the shelf near 68°S.

The volume transport of a bottom plume can increase through entrainment as the plume flows downslope from its source. Entrainment occurs when the current shear across the interface between the upper surface of the plume and the ambient water is sufficient to generate breaking internal waves which mix ambient water into the plume, increasing its volume in the downslope direction. Because of the low temperatures associated with the Weddell Sea plumes the plume density actually increases with increasing depth (the thermobaric effect) so that buoyant forcing increases downslope and the overall plume transport increases. *Killworth* [1977] provided an excellent summary of previous work on Weddell Sea Bottom Water formation, and developed a model for downslope plume dynamics which incorporated pressure-dependent terms in the equation of state. His results were consistent with a 200–300% increase, through entrainment during downslope flow, in the initial volume of water formed on the continental shelves and yielded a transport of about 1.5×10^6 m^3 s^{-1} along the 200 m isobath. *Alendahl et al.* [1994] have developed a full equation of state, entrainment-based, variable drag coefficient model for the behaviour of plumes when descending a slope which yields a 400% volume transport increase through entrainment. Given an input of 10^6 m^3 s^{-1} from the Filchner-Ronne Ice Shelf system, their model predicts a total volume transport in excess of 2–3 $\times$ 10^6 m^3 s^{-1} at less than 1500 m depth downstream from the ice shelves. Use of the variable drag coefficient therefore yields a greater volume transport than the 1–1.5 $\times$ 10^6 m^3 s^{-1} predicted at 2000 m by *Killworth* [1977].

The near-bottom distributions of potential temperature and salinity suggest the presence at, or deeper than, about 2500 m on transect 2 of a cold core which was slightly less saline than water to the east or west (Figure 12). A similar, although slightly warmer, T minimum was also present at 2500 m on transect 3, but the salinity minimum was present in deeper water at about 2800 m (Figure 12). The highest near-bottom salinities observed on transect 2 (nearly 34.65 psu) occurred at about the 2000-m isobath. This feature was not observed at transect 3, and nowhere on this transect was the salinity as high as 34.65 psu. This near-bottom T and S structure at 2000–2500 m was accompanied by a weak but

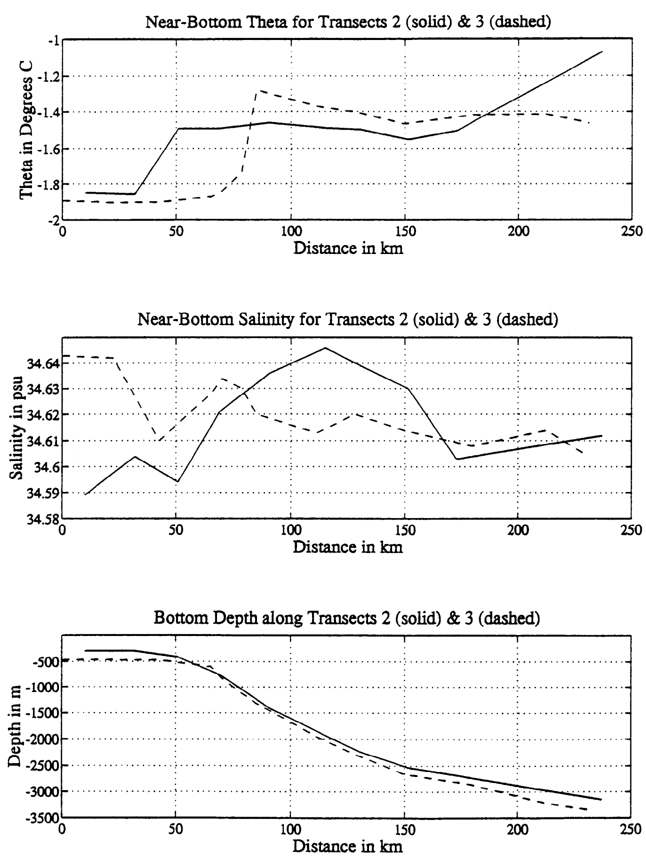

Figure 12. Near-bottom values of potential (top) temperature and (middle) salinity at zonal transects 2 (solid) and 3 (dashed). Bottom panel shows bottom depths for the two transects.

persistent deep current speed maximum which was higher at transect 3 than at transect 2. Transect 4, though incomplete, was contoured consistent with presence of such a feature there as well. If we assume for the sake of discussion that this *T/S*/current feature was a discrete plume about 50 km wide, 500 m thick and with a mean northward speed of 8 cm s^{-1} at transect 2, then the associated northward transport would have been about 2×10^6 m^3 s^{-1} at that transect. Increased northward current speeds at transect 3 would have increased the northward transport there by about 0.4×10^6 m^3 s^{-1}. These estimates are admittedly rough, given the coarse station spacing combined with the sloping bottom, but the data are clearly consistent with a northward transport of $1\text{–}2 \times 10^6$ m^3 s^{-1}.

A 2000–2500 m deep bottom plume was present during at least one other time period. *Anderson et al.* [1991] presented anthropogenic carbon dioxide concentration data, obtained during 1988–1989 along a cross-slope transect off Joinville Island, which showed peak concentrations exceeding 20 μmoles kg^{-1} in a band about 100 km wide centered at about the 2000 m isobath on the continental slope. They speculated that this band, which was not observed on a cross-slope transect farther south off the Ronne Ice Shelf, represented input from the shelf along the Antarctic Peninsula and more specifically from the Larson Ice Shelf. The increase in northward transport which we observed between transects 2 and 3 might reflect Larson Ice Shelf input. This increase cannot, however, be interpreted solely in terms of ice shelf input because it coincided with the general increase in northward transport between transects 2 to 3 which we have previously attributed to inflow from the east. The concept of significant Larson Ice Shelf input is supported, also, by the observed increase in northward flow along the shelf break off the Ice Shelf between transects 2 and 3.

Acknowledgments. This work has been carried out with the support of National Science Foundations grants OPP-9024828 to Science Applications International Corporation (R.D.M.) and OPP-9024755 and OPP-9313700 to Columbia University (A.L.G.). Helpful advice in preparing the manuscript was received from Laurie Padman of Oregon State University. John Gunn of SAIC provided invaluable assistance in carrying out the transport computations. Bruce Huber of LDEO aided in preparation of the CTD graphics and provided early access to processed data. Eberhard Fahrbach of the Alfred-Wegener-Institute for Ocean and Polar Research in Bremerhaven provided plots of his time series current data which were useful for comparison with our results. We are grateful, finally, to Eberhard Fahrbach and to two anonymous reviewers for their constructive comments. This is Lamont-Doherty Earth Observatory contribution 5334.

References

Alendal, G., H. Drange, and P. M. Haugan, Modelling of deep-sea gravity currents using an integrated plume model, *The Role of the Polar Oceans in Shaping the Global Environment: The Nansen Centennial Volume*, pp. 237–246, AGU Washington, D. C., 1994.

Anderson, L. G., O. Holby, R. Lindegren, and M. Ohlson, The transport of anthropogenic carbon dioxide into the Weddell Sea, *J. Geophys. Res.*, *96*, 16,679–16,687, 1991.

Andreas, E., M. A. Lange, S. F. Ackley, and P. Wadhams, Roughness of Weddell Sea ice and estimates of the air-ice drag coefficient, *J. Geophys. Res.*, *98*, 12,439–12,452, 1993.

Carmack, E. C., and T. D. Foster, On the flow of water out of the Weddell Sea, *Deep Sea Res.*, *22*, 711–724, 1975.

Deacon, G. E. R., A general account of the hydrology of the South Atlantic Ocean, *Discovery Rep.*, *7*, 171–238, 1933.

Deacon, G. E. R., The Weddell Gyre, *Deep Sea Res.*, *26*, 981–995, 1979.

Fahrbach, E., G. Rohardt, M. Schröder, and V. Strass, Transport and structure of the Weddell Gyre, *Ann. Geophys.*, *12*, 840–855, 1994.

Foldvik, A., T. Gammelsrød, and T. Tørresen, Circulation and water masses on the Southern Weddell Sea Shelf, in *Oceanology of The Antarctic Continental Shelf, Antarctic Res. Ser.*, vol. 43, edited by S. S. Jacobs, pp. 5–34, AGU, Washington, D. C., 1985.

Foreman, M. G. G., Manual for tidal currents analysis and prediction, *Pacific Marine Science Report 78-6*, Institute of Ocean Sciences, Sidney, B.C., Canada, 70 pp., 1978.

Foster, T. D., and E. C. Carmack, Frontal zone mixing and Antarctic Bottom Water formation in the southern Weddell Sea, *Deep Sea Res.*, *23*, 301–317, 1976.

Gill, A. E., Circulation and bottom water formation in the Weddell Sea, *Deep Sea Res.*, *20*, 111–140, 1973.

Gloersen, P., W. J. Campbell, D. J. Cavalieri, J. C. Comiso, C. L. Parkinson, and H. J. Zwally, Arctic and Antarctic sea ice, 1978–1987: Satellite passive-microwave observations and analysis, *NASA Rep.*, *SP-511*, 290 pp., 1992.

Gordon, A. L., E. Molinelli, and T. Baker, Large-scale relative dynamic topography of the Southern Ocean, *J. Geophys. Res.*, *83*, 3023–3032, 1978.

Gordon, A. L., D. G. Martinson, and H. W. Taylor, The wind-driven circulation in the Weddell-Enderby Basin, *Deep Sea Res.*, *28*, 151–163, 1981.

Gordon, A. L., B. A. Huber, H. H. Hellmer, and A. Ffield, Deep and bottom water of the Weddell Sea's western rim, *Science*, *262*, 95–97, 1993.

Hollister, C. D., and R. B. Elder, Contour currents in the Weddell Sea, *Deep Sea Res.*, *16*, 99–101, 1969.

Huber, B. A., P. Mele, and A. Gordon, Report of the Winter Weddell Sea Project, ANT V/2, Hydrographic Data, *Tech. Rep. L-DGO-89-1*, Lamont-Doherty Geol. Obs., Palisades, New York, 1989.

Huber, B. A., P. Mele, W. Haines, A. Gordon, and V. Lukin, Ice Station Weddell 1 CTD/Hydrographic Data, *Tech. Rep. L-DEO-94-2*, Lamont-Doherty Earth Obs., Palisades, New York, 1994.

Ice Station Weddell Group, Weddell Sea exploration from ice station, *Eos Trans. AGU*, *74*, 121 and 124–126, 1993.

Killworth, P. D., Mixing on the Weddell Sea continental slope, *Deep Sea Res.*, *24*, 427–448, 1977.

Limbert, D. W. S., S. J. Morrison, C. B. Sear, P. Wadhams, and M. A. Rowe, Pack-ice motion in the Weddell Sea in relation to weather systems and determination of a Weddell sea sea-ice budget, *Ann. Glaciol.*, *12*, 104–112, 1989.

McPhee, M. G., Analysis and prediction of short-term ice drift, *Trans. ASME J. Offshore Mech. Arctic Eng.*, *110*, 94–100, 1988.

Monin, A. S., and A. M. Yaglom, *Statistical Fluid Mechanics: Mechanics of Turbulence*, MIT Press, Cambridge, Mass., 1971.

Nelson, D. M., W. O. Smith Jr., R. D. Muench, L. I. Gordon, C. W. Sullivan, and D. M. Husby, Particulate matter and nutrient distributions in the ice edge zone of the Weddell Sea; relationship to hydrography during late summer, *Deep Sea Res.*, *36*, 191–209, 1989.

Nowlin, W. D., Jr., and W. Zenk, Westward bottom currents along the margin of the South Shetland Island Arc, *Deep Sea Res.*, *35*, 269–301, 1988.

Orsi, A. H., W. D. Nowlin Jr., and T. Whitworth, III, On the circulation and stratification of the Weddell Gyre, *Deep Sea Res.*, *40*, 169–203, 1993.

Wamser, C., and D. G. Martinson, Drag coefficients for winter Antarctic pack ice, *J. Geophys. Res.*, *98*, 12,431–12,437, 1993.

A. L. Gordon, Lamont-Doherty Earth Observatory, Palisades, NY 10964.

R. D. Muench, Earth & Space Research, 10533 Ravenna Avenue, NE, Seattle, WA 98125-7745.

(Received November 3, 1994; revised February 28, 1995; accepted March 6, 1995.)